Chemical Science

EDGE ARTICLE

View Article Online
View Journal | View Issue

Cite this: *Chem. Sci.*, 2016, **7**, 4329

Symmetry of octa-coordination environment has a substantial influence on dinuclear Tb^{III} triple-decker single-molecule magnets†

Keiichi Katoh,* Brian K. Breedlove and Masahiro Yamashita*

Single-molecule magnet (SMM) properties of terbium(III)-phthalocyaninato and porphyrinato mixed ligand triple-decker complexes, [(TTP)Tb(Pc)Tb(TTP)] (**1**) and [(Pc)Tb(Pc)Tb(TTP)] type (**2**), were studied and were compared with those of the Tb^{III} homoleptic triple-decker complex [(obPc)Tb(obPc)Tb(obPc)] (**3**) in order to elucidate the relationship between octa-coordination environments and SMM properties (Tb^{III} = terbium(III), TTP^{2-} = tetraphenylporphyrinato, Pc^{2-} = phthalocyaninato, $obPc^{2-}$ = 2,3,9,10,16,17,23,24-octabutoxyphthalocyaninato). By combining TTP^{2-} and Pc^{2-} with Tb^{III} ions, it is possible to make three octa-coordination environments: SP–SP, SAP–SP and SAP–SAP sites, where SAP is square-antiprismatic and SP is square-prismatic. The direction and magnitude of the ligand field (LF) strongly affect the magnetic properties. Complexes **2** and **3**, which have SAP–SAP sites, undergo dual magnetic relaxation processes in the low temperature region in a direct current magnetic field. On the other hand, **1**, which has an SP–SP environment, undergoes a single magnetic relaxation process, indicating that the octa-coordination environments strongly influence the SMM properties. The SMM behaviour of dinuclear Tb^{III} SMMs **1–3** were explained by using X-ray crystallography and static and dynamic susceptibility measurements. This work shows that the SMM properties can be fine-tuned by introducing different octa-coordination geometries with the same Tb^{III}–Tb^{III} distances.

Received 4th December 2015
Accepted 7th March 2016

DOI: 10.1039/c5sc04669f

www.rsc.org/chemicalscience

Introduction

The field involving single-molecule magnets (SMMs) began in 1993 with the synthesis of Mn_{12} clusters.[1] In recent years, mononuclear metal complexes, not just polynuclear ones, have also been reported.[2] In other words, slow magnetic relaxation processes are observed for SMMs regardless of the type and number of metal ions in the complexes under certain conditions. In general, in crystals, d and/or f electrons forming the electronic states reflect the symmetry of the crystals. As a result, the crystal field (CF) or ligand field (LF) directly influences the magnetic properties. Recently, a few groups have published reviews on lanthanide(III) (Ln^{III})-based SMMs,[2] which have several distinctive features, including slow magnetic relaxation and quantum tunnelling of the magnetization (QTM). Although the reviews show that molecular design is important to bring about SMM behaviour, controlling the magnetic relaxation pathway is still challenging. Since the tunneling gap (Δ_{tunnel}) is dependent on the establishment of QTM, most studies have focused on the influence of the spin–spin interactions and nuclear spins.[2] However, because molecular spintronics based on SMMs, which exhibit new quantum phenomena, will be the next generation devices,[3] it is necessary to elucidate completely the magnetic relaxation processes of the SMMs used.

In 2003, the terbium(III)-phthalocyaninato stacked complex $(TBA)^+[TbPc_2]^-$ (Tb^{III} = terbium(III), Pc^{2-} = phthalocyaninato, TBA^+ = tetrabutylammonium) was reported to exhibit SMM behaviour, which originates from the ligand field (LF).[4] The magnetic properties of rare-earth metal ions are strongly related to the charge density distribution.[2] Tb^{III} and Dy^{III} ions exhibit uniaxial magnetic anisotropies of the easy axis, and splitting of the ground state multiplets is caused by the LF at the axial position. In this case, the energy gap between the ground and first excited states is associated with the energy barrier for the reversal of the magnetization (Δ), thereby causing slow relaxation of the magnetization. Consequently, the direction and magnitude of the LF strongly affect the magnetic properties.[1–4]

Although lanthanide(III)-phthalocyaninato double-decker ($LnPc_2$) SMMs have been studied in detail, little is known about Ln_2Pc_3. Ishikawa and co-workers have reported a series of studies on the magnetic properties of the Ln^{III}-Pc triple-decker complex [(Pc)Ln(Pc)Ln(obPc)] ($obPc^{2-}$ = 2,3,9,10,16,17,23,24-octabutoxyphthalocyaninato; Ln^{III} = Tb, Dy, and Y), which are the first reports on the dynamic magnetism of a coupled 4f system.[5] More recently, we have reported that the Tb^{III}-Pc triple-decker SMM $Tb_2(obPc)_3$ (**3**) shows dual magnetic relaxation

Department of Chemistry, Graduate School of Science, Tohoku University, 6-3 Aramaki Aza Aoba, Aoba-ku, Sendai, Miyagi 980-8578, Japan. E-mail: kkatoh@m.tohoku.ac.jp

† Electronic supplementary information (ESI) available. CCDC 989974 for **1** and 1041202 for **2**. For ESI and crystallographic data in CIF or other electronic format see DOI: 10.1039/c5sc04669f

processes in the low temperature region in a dc magnetic field (H_{dc}).[6] The dual magnetic relaxation behaviour has been observed not only for **3** but also for the spatially closed Tb^{III}-Pc quadruple- and quintuple-decker complexes.[7] This is clear evidence that the magnetic relaxation mechanism depends heavily on the f–f interactions between the Tb^{III} ions in the dinuclear systems. Several SMMs with dual magnetic relaxation processes have been reported, and it has been shown that dual magnetic relaxation processes are observed for SMMs regardless of the type and number of metal ions in the complexes.[8] It is well known that the magnetic relaxation rates reflect the local molecular symmetry and are extremely sensitive to tiny distortions in the coordination geometries. Our results suggest that the dual magnetic relaxation properties in the Tb^{III}-Pc multiple-decker systems have a magic number of "two", *i.e.*, the number of metal sites.[7] However, further experiments are required to corroborate this hypothesis.

In this study, we focused on a porphyrin (H_2Por) ligand, which has a cyclic structure with four pyrroles in common with a phthalocyanine (H_2Pc). In the case of H_2Por, the four pyrroles in the macrocycle are linked by methine groups, whereas H_2Pc has a four isoindole molecules, which are pyrrole molecules fused with benzene rings, linked with nitrogen atoms. Both have planar structures with the π-conjugation spread over the entire molecule. However, the stacked coordination environments in complexes are significantly different depending on the presence or absence of π-electron repulsion. It is well-known that porphyrins form multiple-decker complexes when coordinated to lanthanide ions. A number of studies on Ln^{III}-Por^{2-} and Ln^{III}-Por^{2-}/Pc^{2-} mixed multiple-decker type SMMs have been reported.[9] From previous research, when using Por^{2-} ligands, the SMM properties are not as same as those of Pc^{2-} complexes due to the LF potential of coordination geometry. In addition, contractions of the square-antiprismatic (SAP) coordination environment affect the LF of the Ln^{III} ions, which in turn affects the SMM properties.[4,9a] However, not only the effects of the ground state for different octa-coordination geometries but also dual magnetic relaxation processes have not been methodically discussed. In order to simplify the discussion, therefore, we designed dinuclear Tb^{III} triple-decker complexes with different octa-coordination environments but with similar intramolecular Tb^{III}–Tb^{III} distances (~0.36 nm). The combination of Por^{2-} and Pc^{2-} with Ln^{III} ions can give rise to three different octa-coordination environments (Scheme 1).

Herein we present the results of studies on the SMM properties of dinuclear Tb^{III} triple-decker mixed ligands complexes [(TTP)Tb(Pc)Tb(TTP)] (**1**) and [(Pc)Tb(Pc)Tb(TTP)] (**2**) (Scheme 1). The relationship between the octa-coordination environment and SMM properties of **1** and **2** are discussed in comparison to Tb_2(obPc)$_3$ (**3**).[6] The SMM behaviours of dinuclear Tb^{III} complexes **1–3** were explained by using X-ray crystallography and static and dynamic susceptibility measurements. This work shows that the SMM properties can be fine-tuned by introducing different octa-coordination geometries while maintaining the same Tb^{III}–Tb^{III} distances.

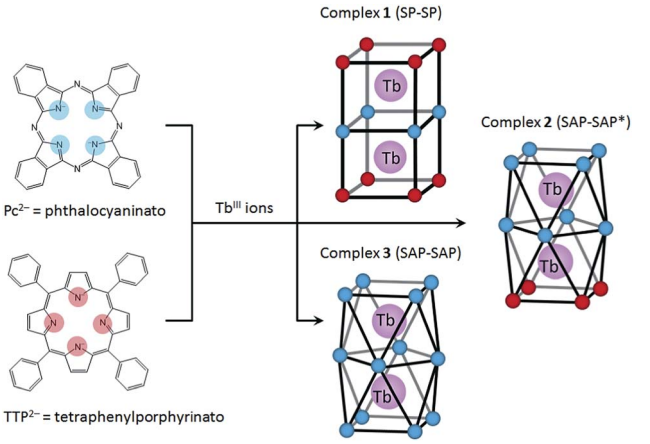

Scheme 1 Schematic illustration of dinuclear Tb^{III} triple-decker complexes **1–3**, which show the three octa-coordination environments: SP–SP, SAP–SAP* and SAP–SAP, respectively, where SAP = square-antiprismatic and SP = square-prismatic.

Experimental

All reagents were purchased from Wako chemicals, Tokyo Chemical Industry (TCI), and Sigma Aldrich and used without further purification. The compounds were prepared following reported procedures with slight modifications.[10]

Synthesis of [(TTP)Tb(Pc)Tb(TTP)] (1) and [(Pc)Tb(Pc)Tb(TTP)] (2)[10]

$Tb(acac)_3 \cdot 4H_2O$ (180 mg, 0.40 mmol) and H_2TTP (tetraphenylporphyrin) (150 mg, 0.25 mmol) were added to dry 1,2,4-trichlorobenzene (40 mL). The solution was refluxed under argon for 4 h. After cooling, Li_2Pc (158 mg, 0.60 mmol) was added to the mixture. Then the solution was refluxed for 12 h. After cooling, the reaction mixture was added to *n*-hexane (500 mL). The obtained solid was purified by using column chromatography on silica gel with chloroform as the eluent. [(TTP)Tb(Pc)Tb(TTP)] (**1**) was obtained from a deep brownish red fraction, which was the first fraction, by removing the solvent, and [(Pc)Tb(Pc)Tb(TTP)] (**2**) was obtained from the dark green second fraction. Column chromatography (C-200 silica gel, Wako and Sephadex G-10, Pharmacia Biotech) was used to remove the remaining impurities. Dark red fine block crystals of **1** were obtained from chloroform/*n*-hexane (50 mg). ESI-MS: *m*/*z* (%): 2055.46605 (100) [M^+]; elemental analysis calcd (%) for $C_{120}H_{72}N_{16}Tb_2 \cdot 3.5CHCl_3$: C 59.97, H 3.08, N 9.06; found: C 60.03, H 3.21, N 8.89. Black fine needle crystals of **2** were obtained from chloroform/*n*-hexane (40 mg). ESI-MS: *m*/*z* (%): 1855.30261 (100) [M^+]; elemental analysis calcd (%) for $C_{108}H_{60}N_{20}Tb_2 \cdot CHCl_3$: C 63.09, H 2.96, N 13.50; found: C 62.91, H 3.28, N 13.36.

Physical property measurements

UV-Vis-NIR spectra for chloroform solutions of **1** and **2** were acquired on a SHIMADZU UV-3100PC in a quartz cell with a pathlength of 1 cm at 298 K (Fig. S1†). IR spectroscopy was

performed on KBr pellets on a Jasco FT/IR-4200 spectrometer at 298 K (Fig. S2†). Electrospray ionization mass spectroscopy and elemental analyses were performed at the Research and Analytical Centre for Giant Molecules, Tohoku University. Magnetic susceptibility measurements were performed on Quantum Design SQUID magnetometers MPMS-3. Direct current (dc) measurements were performed in the temperature (T) range of 1.8–300 K and in dc magnetic fields (H_{dc}) of −70 000 to 70 000 Oe. Alternating current (ac) measurements were performed in the ac frequency (ν) range of 1–996 Hz with an ac field amplitude of 3 Oe in the presence of a dc field (zero–6000 Oe). Measurements were performed on randomly oriented powder samples of **1–3**, which were placed in gel capsules and fixed with *n*-eicosane to prevent them from moving during measurements. All data were corrected for the sample holder, *n*-eicosane, and diamagnetic contributions from the molecules by using Pascal's constants.

X-Ray crystal structure analysis

A single crystal was mounted on a loop rod coated with Paratone-N (HAMPTON RESEARCH). Data collection was performed on a Rigaku Saturn 724+ CCD diffractometer with graphite-monochromated Mo-Kα radiation ($\lambda = 0.71069$ Å) at $T = -180 \pm 1$ °C. An empirical absorption correction based on azimuthal scans of several reflections was applied. The data were corrected for Lorentz and polarization effects. All non-hydrogen atoms were refined anisotropically using a least-squares method, and hydrogen atoms were fixed at calculated positions and refined using a riding model. SHELXL-97 was used for structure refinement, and the structure was expanded using Fourier techniques.[12a] The weighting scheme was based on counting statistics. Full-matrix least-squares refinements on F^2 based on unique reflections with unweighted and weighted agreement factors of $R = \sum||F_o| - |F_c||/\sum|F_o|$ ($I > 2.00\sigma(I)$), and $wR = [\sum w(F_o^2 - F_c^2)^2/\sum w(F_o^2)^2]^{1/2}$ were performed. Powder X-ray diffraction (PXRD) patterns of crushed polycrystalline samples of **1** and **2**, loaded into capillaries (diameter: 0.8 mm, length: 80 mm, Hilgenderg) with their mother liquor, were collected at 298 K using a Rigaku X-ray diffractometer (AFC-7R/LW) operated at 50 kV and 300 mA in the diffraction angle (2θ) range of 3–60° in steps of 0.02° at 2 s per step (Fig. S3†). Visualization and analysis of the crystal structures and PXRD patterns were simulated from the single crystal data by using Mercury 3.0.[12b]

Results and discussion

Synthesis and electronic structure

The structures of **1–3** are shown in Fig. 1 with several octa-coordination geometries for Tb^{III} dinuclear systems. In our studies, we used a tetraphenylporphyrinato (TTP^{2-}) ligand with a phthalocyaninato (Pc^{2-}) ligand because it has a high solubility, making crystallization easier.[10] In order to control the spin orientation in the molecules, we designed **1–3** so that the two Tb^{III} ions were along the anisotropy axis. Mixed ligand triple-decker complexes **1** and **2** were synthesized in one-step using $Tb(acac)_3 \cdot nH_2O$, H_2TTP and Li_2Pc following a procedure

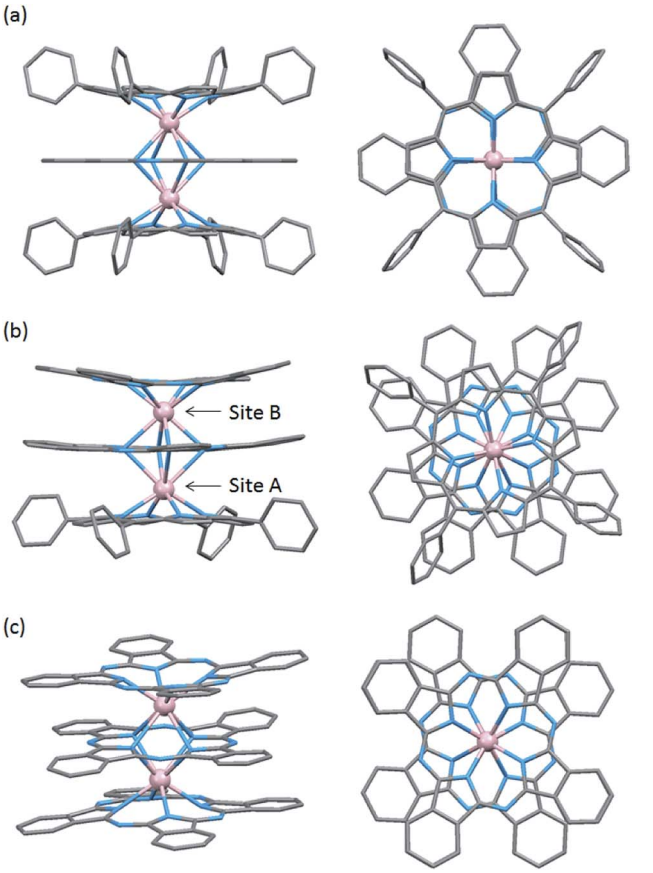

Fig. 1 Crystal structure of (a) **1** (SP–SP), (b) **2** (SAP–SAP*) and (c) **3** (SAP–SAP): (left) side view and (right) top view. Proton and *n*-butoxy substituents of **3** omitted for clarity. Tb^{III}: pink, C: grey, and N: light blue.

reported by Weiss and co-workers.[10] On the other hand, triple-decker **3** was synthesized in one step starting from $Tb(acac)_3 \cdot 4H_2O$ and H_2obPc following a procedure reported by Takahashi and co-workers.[11] Por^{2-} and Pc^{2-} can form neutral triple-decker complexes composed of two Tb^{III} ions and three $obPc^{2-}$ ligands ([(obPc)Tb(obPc)Tb(obPc)] (**3**)) and in Por^{2-}:Pc^{2-} ratios of 1:2 ([(Pc)Tb(Pc)Tb(Por)] (**2**)) and 2:1 ([(Por)Tb(Pc)Tb(Por)] (**1**)) with closed shell π electron systems.[5,6,9–11]

Triple-decker complexes **1–3** are soluble in most organic solvents, except for alcohols and *n*-hexane. A chloroform solution of **1–3** showed 3–6 prominent absorption bands in the wavelength range of 250–1200 nm (Fig. S1†). The absorption spectrum of **1**, which has an inner Pc^{2-} ligand strongly interacting with the two outer TTP^{2-} ligands, were similar to those of the [(TTP)Ln(Pc)Ln(TTP)] analogues and, therefore, were assigned on the basis of a previous report.[10] The strong absorption bands at 419 nm were assigned to be Soret (S) bands, and the weak absorptions at 493 and 553 nm were assigned to be the Q bands of the TTP^{2-} ligands with a large contribution from the former tetrapyrroles, respectively. The bands at 353 (S band) and 606 nm (Q band) were attributed to the Pc^{2-} ligand. Furthermore, the weak broad bands in the near-IR region (850–1100 nm) were assigned to be electronic transitions between the dianionic ligands.

The absorption spectrum of **2** was similar to that of **1**, but the absorption intensities and peak positions were different. From experimental and theoretical studies, this is clear evidence that excitonic interactions between the two Pc^{2-}/Por^{2-} chromophores depend heavily on the molecular structures, in which the ligands are stacked in a staggered face-to-face fashion.[10] The strong absorption bands at 341 nm with shoulders at 324 nm, and the weak absorptions at 617 and 669 nm were assigned to be S and Q bands of the Pc^{2-} ligands, respectively. The bands at 418 (S band) and those at 522 and 604 nm (Q bands) were attributed to the TTP^{2-} ligand. Furthermore, the broad band at 737 nm was assigned to be electronic transitions between the dianionic ligands. In IR spectra of **1** and **2**, three strong peaks at 1330, 1062, 728 cm^{-1}, which were attributed to the Pc^{2-} ligand, were observed (Fig. S2†).

In the case of **3**, the two absorption bands at 290 and 356 nm were assigned to be the S bands of the obPc^{2-} ligands,[11] and those at 577 and 655 nm were assigned to be the Q bands of the obPc^{2-} ligands.

Crystal structure and octa-coordination geometry

To evaluate the effects of the coordination geometry around the Tb^{III} ion in the triple-decker complexes **1–3**, contractions of their octa-coordination environments were investigated by using single-crystal X-ray diffraction analysis (Fig. 1). The longitudinally contracted SAP coordination environment shares an edge with an undistorted complex, *i.e.*, there is a twist angle (φ) between the upper and the lower Pc^{2-} ligands (Fig. S4†). Selected crystallographic data for **1–3** are compiled in Table S1.† The data clearly show that contractions of the octa-coordination environment have an influence on the LF of the Ln^{III} ions, which affects the SMM properties.[4,9,13]

Complex **1**, shown in Fig. 1a, crystallized with chloroform in the crystal lattice in the tetragonal space group $I4/m$, which has a SP (quasi-D_{4h}) coordination environment (Scheme 1 and Fig. S4d†). Complex **1** has two Tb^{III} ions, which a Pc^{2-} ligand coordinated between them. The inner Pc^{2-} ligand with four isoindole-nitrogen donor atoms (N_{iso}) and a center of symmetry strongly interacts with the two outer TTP^{2-} ligands. The center of the square formed by the four pyrrolic nitrogens of the Pc^{2-} ligand form a crystallographically imposed inversion center, making the two Tb^{III} ions and outer TTP^{2-} ligands equivalent. In addition, the inner Pc^{2-} ligand of **1** is located on a mirror plane. The intramolecular Tb^{III}–Tb^{III} distance was determined to be 0.372 nm (Tb^{III}–Tb^{III} distance was determined to be 0.352 nm in **3**).[6] φ between the outer TTP^{2-} ligands and the inner Pc^{2-} ligand was determined to be 3.62°. Thus, the two Tb^{III} sites in **1** have a slightly distorted SP geometry (Fig. 1a). The Tb^{III} ions are unevenly spaced between the outer TTP^{2-} and inner Pc^{2-} ligands with distances of 0.239 nm (**3**: 0.234–0.237 nm)[6] from the mean plane of the four N_{iso} of the outer TTP^{2-} ligands and 0.268 nm (**3**: 0.258–0.262 nm)[6] from the mean plane of the four N_{iso} of the inner Pc^{2-} ligand.

Crystal-packing diagrams of **1** are shown in Fig. S5.† The intermolecular $Tb^{III}\cdots Tb^{III}$ distance along the *a* and *c* axes were determined to be 1.431 and 1.364 nm, respectively. Each molecule of **1** is rather well separated from neighboring molecules due to the tetraphenyl groups of TTP^{2-} ligands and chloroform molecules as crystal solvents. Furthermore, PXRD patterns for **1** at 293 K are similar to those simulated from X-ray single crystallographic data for **1** at 93 K (Fig. S3-1†).

Recently, Jiang and co-workers have reported the [(Por)Ln(Pc)Ln(Por)] type triple-decker SMM {(TCIPP)Dy[Pc(OBNP)$_4$]Dy(TCIPP)}, which has Dy^{III} ions in SAP ($\varphi \approx 7°$) and SAP* ($\varphi \approx 42°$) environments (TClPP = *meso*-tetrakis(4-chlorophenyl)porphyrinato; Pc(OBNP)$_4$ = tetrakis(dinaphtho[1,2-*e*:1′,2′-*g*]-1,4-dioxocine)[2,3-*b*;2′,3′-*k*;2″,3″-*t*;2‴,3‴-*c*′]phthalocyaninato).[9e] The coordination environments are completely different from those in **1**, which has two Tb^{III} ions in the slightly distorted SP environments ($\varphi \approx 4°$).

On the other hand, complex **2**, shown in Fig. 1b, crystallized with chloroform in the crystal lattice in the monoclinic space group $P2_1/c$. **2** has a SAP (quasi-D_{4d}) coordination environment (Scheme 1 and Fig. S4e†), and it has two Tb^{III} ions and an inner Pc^{2-} ligand, which strongly interact with each other. The Tb^{III}–Tb^{III} distance in **2** was determined to be 0.363 nm, and φ between the outer Pc^{2-} ligands and the center Pc^{2-} one was determined to be 38.40° (site B = SAP*). On the other hand, φ between the outer TTP^{2-} ligands and the inner Pc^{2-} one was determined to be 13.80° (site A = SAP). The Tb^{III} ions are unevenly spaced between the outer TTP^{2-} and inner Pc^{2-} ligands with distances of 0.237–0.240 nm from the mean plane of the four N_{iso} of the outer TTP^{2-} ligands and 0.270–0.274 nm from the mean plane of the four N_{iso} of the inner Pc^{2-} one. On the other hand, the Tb^{III} ions are unevenly spaced between the outer Pc^{2-} and inner Pc^{2-} ligands with distances of 0.235–0.237 nm from the mean plane of the four N_{iso} of the outer Pc^{2-} ligands and 0.257–0.260 nm from the mean plane of the four N_{iso} of the center Pc^{2-} one. The distance between the Tb^{III} ions and N_{iso} of **1–3** are essentially the same.

Crystal-packing diagrams of **2** are shown in Fig. S6.† The closest intermolecular $Tb^{III}\cdots Tb^{III}$ distance along the *c* axis was determined to be 1.162 nm. Each molecule of **2** is rather well separated from neighboring molecules due to the four phenyl groups of the TTP^{2-} ligands and chloroform as crystal solvents. PXRD patterns of **2** at 293 K were similar to the patterns simulated from X-ray single crystallographic data of **2** at 93 K (Fig. S3-2†).

A number of studies on [(Pc)Ln(Pc)Ln(Por)] mixed ligand triple-decker type SMMs have been reported.[9a,9d] Ishikawa and co-workers reported the triple-decker complex {(Pc)Tb(Pc)Tb[T(*p*-OMe)PP]} [T(*p*-OMe)PP = 5,10,15,20-tetra(*p*-methoxyphenyl)porphyrinato], in which the Tb^{III} ions are in SP ($\varphi \approx 1°$) and SAP ($\varphi \approx 45°$) environments.[9a] Jiang and co-workers reported the triple-decker complex {(TClPP)Dy[Pc(OPh)$_8$]Dy[Pc(OPh)$_8$]} [Pc(OPh)$_8$ = 2,3,9,10,16,17,23,24-octa(phenoxyl)-phthalocyaninato] with Dy^{III} ions in SAP ($\varphi \approx 10°$) and SAP* ($\varphi \approx 25°$) environments.[9d] From a comparison of the reported complexes, in **2**, the Tb^{III} ions have SAP ($\varphi \approx 14°$) and SAP* ($\varphi \approx 38°$) environments, and the octa-coordination environments are completely different from those in **1** (SP–SP). In other words, both Tb^{III} sites in **2** exhibit slightly distorted SAP geometries with independent environments (Fig. 1b). Viewed from another direction, site A ($\varphi \approx 14°$) appears to have a slightly distorted SP

Table 1 Selected crystallographic data for dinuclear Ln^{III} triple-decker mixed ligand complexes

Complexes	Ln–Ln distance/nm	φ_A/°	φ_B/°	Site geometry
[(TTP)Tb(Pc)Tb(TTP)] **1**[a]	0.372	4	4	SP–SP
[(Pc)Tb(Pc)Tb(TTP)] **2**[a]	0.363	14	38	SAP–SAP*
[(obPc)Tb(obPc)Tb(obPc)] **3**[6]	0.352	32	32	SAP–SAP
{(Pc)Tb(Pc)Tb[T(*p*-OMe)PP]}[9a]	0.360	1	45	SP–SAP
{(TCIPP)Dy[Pc(OBNP)$_4$]Dy(TCIPP)}[9e]	0.371	7	42	SAP–SAP*
{(TCIPP)Dy[Pc(OPh)$_8$]Dy[Pc(OPh)$_8$]}[9d]	0.361	10	25	SAP–SAP*

[a] This work; see main text in this manuscript.

environment. Thus, the SMM properties cannot be predicted solely from the crystal structure, and it is necessary to study the SMM properties in detail (see Magnetic properties section).

We have already reported a crystal structure of **3**.[6] Complex **3** crystallized with ethanol in the crystal lattice in the triclinic space group $P\bar{1}$, as shown in Fig. 1c. Complex **3** has two Tb^{III} ions sandwiched between three $obPc^{2-}$ ligands with four N_{iso} donor atoms and a center of symmetry. The intramolecular Tb^{III}–Tb^{III} distance was determined to be 0.352 nm. φ between the outer $obPc^{2-}$ ligands and the inner one was determined to be 32°. This means that both Tb^{III} sites in **3** have the same slightly distorted SAP geometry (quasi-D_{4d}). The intermolecular $Tb^{III}\cdots Tb^{III}$ distance along the *a* axis was determined to be 1.098 nm. Each molecule of **3** is rather well separated from neighbouring molecules due to the *n*-butoxy chains. This is supported by the dc and ac magnetic measurements on an isomorphous sample of **3** diluted with diamagnetic $Y_2(obPc)_3$, which show that the intermolecular magnetic interactions are negligible. In other words, the magnetic properties of **1–3** are due to intramolecular Tb^{III}–Tb^{III} interactions and the symmetry of the octa-coordination geometry (*vide infra*). Selected molecular geometry information for dinuclear Ln^{III} triple-decker mixed ligand complexes are listed in Table 1.

Static magnetic properties

In order to understand the SMM properties of **1** (SP–SP) and **2** (SAP–SAP*), we compared them with those of SMM **3** (SAP–SAP).[6] The dc magnetic susceptibilities (χ_M) of powder samples of **1** and **2** were measured in the temperature (T) range of 1.8–300 K in a dc magnetic field (H_{dc}) of 500 Oe by using a superconducting quantum interference device (SQUID) magnetometer.

The $\chi_M T$ value at 300 K (23.6 cm^3 K mol^{-1}) corresponds to two free Tb^{III} ions ($^7F_6$, $S = 3$, $L = 3$, $g = 4/3$) (Fig. 2a). The χ_M of **1** obeyed the Curie–Weiss law, giving a Curie constant (C) of 23.3 cm^3 K mol^{-1} with a positive Weiss constant (θ) of 0.15 K over the T range of 180–300 K (Fig. S7a†). With a decrease in T, the $\chi_M T$ value of **1** gradually increased and reached ~25 cm^3 K mol^{-1} at 1.8 K. In the case of **2**, the $\chi_M T$ value at 300 K (23.6 cm^3 K mol^{-1}) corresponds to two free Tb^{III} ions (Fig. 2a). The χ_M obeyed the Curie–Weiss law, giving a C value of 23.6 cm^3 K mol^{-1} with a positive θ of 0.02 K over the entire T range (Fig. S7b†). With a decrease in T, the $\chi_M T$ value of **2** slightly increased and

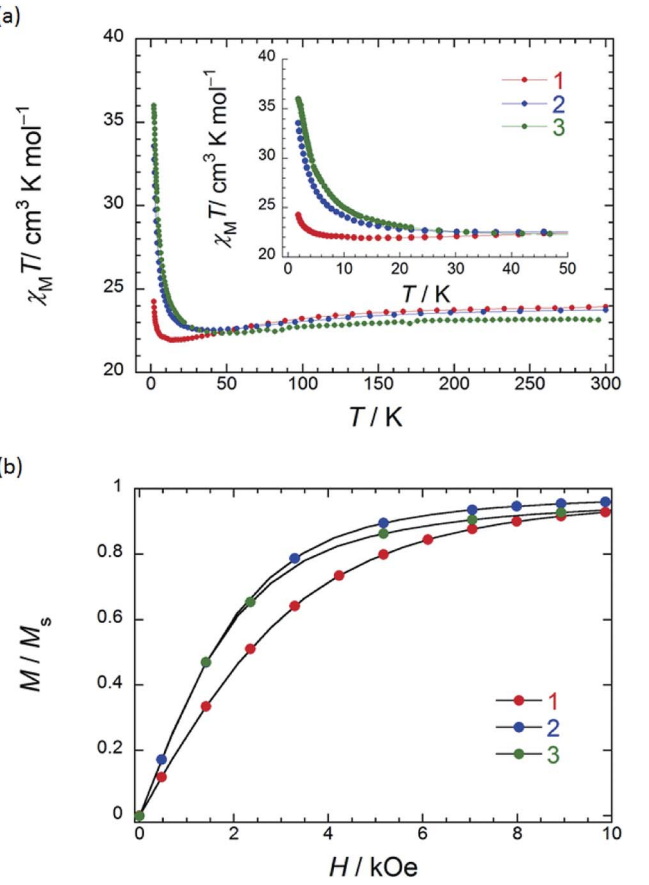

Fig. 2 (a) Temperature (T) dependence of $\chi_M T$ measured on powder samples of **1** (SP–SP), **2** (SAP–SAP*) and **3** (SAP–SAP) at 500 Oe. (b) Normalised magnetization *versus* field (M/M_s *versus* H) performed on powder samples of **1–3**. The solid lines are guides for eyes.

reached 34 cm^3 K mol^{-1} at 1.8 K. The behaviour of $\chi_M T$ clearly shows that the magnetic behaviour depends heavily on the magnetic dipole–dipole interactions between the Tb^{III} ions in the molecule under 10 K. Behaviour similar to those of triple-decker **3** was observed, as shown in Fig. 2a.[6] $\chi_M T$ *versus* T plots for **3** increased with a decrease in T and reached a maximum of 36 cm^3 K mol^{-1} at 1.8 K, which indicates the existence of ferromagnetic interactions between the Tb^{III} ions.[5–7] **1** has a lower $\chi_M T$ value at 1.8 K than **2** and **3** do. The deviation in the $\chi_M T$ values occur due to a combination of a few factors, such as the intermetallic Tb^{III}–Tb^{III} distance, LF effects with significant magnetic anisotropy, and/or depopulation of the excited states.[2b–e,g,h,5–7,9a]

To understand the deviation in the $\chi_M T$ value of **1**, we first studied the influence of the Tb^{III}–Tb^{III} distance. The intramolecular Tb^{III}–Tb^{III} distance of complexes **1–3** were determined to be in the range of 0.352–0.372 nm, indicating that there were strong magnetic interactions between Tb^{III} ions in the molecules. This is clear evidence that the $\chi_M T$ value of Tb^{III} dinuclear systems depends heavily on the magnetic dipole–dipole (f–f) interactions between the Tb^{III} ions.[5–7] Therefore, the ferromagnetic dipole–dipole interactions ($D_{ij} \propto 1/r_{ij}^3$, where r_{ij} is the distance between spin i and j) between the Tb^{III} ions in **1**

are similar to those in triple-decker complex **3** because r_{ij} between the Tb^{III} ions of **1** (0.372 nm) is similar to that of **3** (0.352 nm) (*ca.* 1/1.1).[6] In other words, the $\chi_M T$ value of **1** cannot be explained solely on the basis of the Tb^{III}–Tb^{III} distance, and it is possible that the magnetic anisotropies of **1–3** are due to the octa-coordination geometries of the Tb^{III} ions.

Next, we focused on the different octa-coordination environments of **1–3**. To study the effects on the magnetic properties of the triple-decker complexes, contractions of the coordination environments in **1** and **2** were investigated. From XRD analysis, it was determined that the octa-coordination geometries of **1** (SP–SP), **2** (SAP–SAP*), and **3** (SAP–SAP) had pseudo-4-fold axes (direction of the uniaxial magnetic anisotropy) perpendicular to the tetrapyrrole rings. In addition, contractions of the SAP coordination environments affect the LF of the Ln^{III} ions, which affects the SMM properties.[4,9a,13] It has been reported that the LF parameters (B_k^q) of an ideal SAP coordination geometry with D_{4d} symmetry is different from B_k^q of an SP coordination geometry with D_{4h} symmetry.[4,9a,13] Differences in the SMM properties are thought to be due to the presence or absence of particular off-diagonal LF terms. Thus, SAP geometry only occurs in the terms B_2^0 ($\alpha_2 A_2^0 r^2$), B_4^0 ($\alpha_4 A_4^0 r^4$) and B_6^0 ($\alpha_6 A_6^0 r^6$), which are LF parameters for the axial anisotropy, where the $\alpha_k A_k^q r^k$ are LF parameters.[13] The LF Hamiltonian can be written as $\hat{H}_{LF} = \sum\sum_{q=-k}^{k} B_k^q O_k^q$, where O_k^q are spin operators.[13] On the other hand, SP geometry not only contributes to the LF of axial parameters but also to the terms B_4^4 ($\alpha_4 A_4^4 r^4$) and B_6^4 ($\alpha_6 A_6^4 r^6$), which are LF parameters for the transverse anisotropy. The fourth-range extradiagonal parameters (B_4^4 and B_6^4) enable mixing between the ground state of the $|+6\rangle$ and $|-6\rangle$ doublet in a zero magnetic field.[4,9a,13] It exerts a greater effect on both the hyperfine structure of the ground state and the ground state multiplets structure.

There have been many attempts to elucidate the relationship between the coordination geometry and LF parameters both experimentally and theoretically. The LF parameters have been shown to have a significant influence on the ground state multiplets structure and magnetic anisotropy. The effects of the LF parameters on the uniaxial anisotropy are described below.

Gatteschi and co-workers have reported that the twist angle (φ) has a big effect on the ground state and the first excited state of the octa-coordination geometries with C_4 symmetry axes for Ln^{III} complexes, since the structures deviate from D_{4d} symmetry. This deviation appears in the fourth-range extradiagonal parameters, and the distortion has an effect on both axial and transverse parameters, which has been shown by using theoretical calculations.[13e] In addition, the angles (α) between the C_4 axis and the direction of Ln^{III}–N_{iso} coordination bond have a strong influence on the LF parameters.[13f]

Ishikawa and co-workers have reported that the values of the energy barrier for the reversal of the magnetization (Δ) of the ground state multiplets of $[TbPc_2]^{+/-}$ complexes are changed depending on the difference in the closest Pc–Pc distance.[4] Longitudinal contraction of the SAP structure causes the changes in Δ and increases the LF splitting of the ground multiplets of Ln^{III} ions in the cation structure.[4i] Furthermore, Ishikawa and co-workers have reported the LF parameters of the Y^{III}–Tb^{III} triple-decker complex [(Pc)Y(Pc)Tb(obPc)] which has quasi-D_{4d} geometry like **3**.[5c] They do not report φ for the Tb^{III} site, but it should be *ca.* 32° on the basis of the structure of a similar complex.[5d] The value of $A_2^0 r^2$ decreases with a decrease in φ from 414 cm^{-1} for $[TbPc_2]^-$ with $\varphi \approx 45°$ to 293 cm^{-1} for [(Pc)Y(Pc)Tb(obPc)] with $\varphi \approx 32°$. It should be noted that the $A_4^4 r^4$ dramatically increases from 10 to 863 cm^{-1}, and $A_6^4 r^6$ increases from a negligible value to 357 cm^{-1}.[4,5c,13j] The Δ value for [(Pc)Y(Pc)Tb(obPc)] with $\varphi \approx 32°$ has been determined to be 300 cm^{-1} from the LF parameters.[5c] On the other hand, Δ for $[TbPc_2]^-$ with $\varphi \approx 45°$ has been determined to be *ca.* 420 cm^{-1} from the LF parameters.[4] Theoretical calculations support the relationship between the LF parameters and Δ.[13g,h] Furthermore, they demonstrate that they can reversibly switch between the non-SMM protonated form $[TbH(TTP)_2]$ with a hepta-coordinate environment to the SMM deprotonated form $[Tb(TTP)_2]^-$ $(H\text{-}DBU)^+$ with D_{4d} symmetry.[9b] They argue that the change in SMM properties is due to the off-diagonal LF term and/or that the lowest energy level is no longer $J_z = \pm 6$ in the hepta-coordinate environment. Therefore, there is a loss of uniaxial anisotropy, and $[TbH(TTP)_2]$ does not exhibit SMM behaviour.

Recently, Chibotaru, Tong and co-workers have reported strong evidence for the relationship between the symmetry and Δ of SMMs.[13g] They demonstrated that when Δ of an Dy^{III} SMM was decreased by changing symmetry from quasi-D_{5h} to quasi-O_h. They report that Δ changes by two orders of magnitude between the quasi-D_{5h} (305 cm^{-1}) and quasi-O_h structures (negligible value). The axial parameters B_2^0 and B_4^0 of quasi-D_{5h} structure are large, whereas the values of the non-axial parameters B_2^2, B_4^4 and B_4^3 of quasi-O_h structure are the same or slightly larger than those of the axial ones. In addition, the Dy^{III} site in the quasi-D_{5h} structure exhibits very strong axial magnetic anisotropy. On the other hand, the Dy^{III} site in the quasi-O_h structure shows weak axial magnetic anisotropy due to the non-axial parameters. In other words, the uniaxial anisotropy of the quasi-D_{5h} structure is stronger than that of quasi-O_h structure on the basis of the *g* tensor.

Considering the above research results, it is possible that the transverse anisotropy parameters (B_k^q; $q \neq 0$) have an effect on the uniaxial magnetic anisotropies and the ground state multiplets structure. The coefficient values show that there are interactions between the metal orbitals and the ligands, and they can be determined experimentally.[2,4,5,9,13] However, we discuss this point in the section "Dynamic magnetic properties".

In order to qualitatively estimate the magnetic anisotropy, reduced magnetization measurements were performed on **1** (SP–SP), **2** (SAP–SAP*), and **3** (SAP–SAP) (Fig. S8-1†). If molecules have large magnetic anisotropies, *M versus* HT^{-1} plots do not overlap on a single curve, and they did not show saturation at high fields (up to 70 kOe).[1,2] *M* of **3** was not synchronised, whereas those of **2** and **1** slightly unaligned, indicating the presence of significant magnetic anisotropy.[13h] To elucidate the ground state of **1–3**, as shown in Fig. 2b, we focused on the initial increase in *M* in a weak dc magnetic field (*M versus H*). *M* of **1** gradually increased, whereas those of **2** and **3** sharply increased. The *M*–*H* curve reflects the overall effect of the LF and

magnetic interactions. As the ground states are rather differently mixed, it is very difficult to infer the strength of the magnetic interactions in various LFs from the M data which have strong magnetic anisotropies. It is indicated that the ground state of **1** is different from that of **2** and **3**. This result agrees with other information concerning the ground state (see Dynamic magnetic properties and Magnetic relaxation mechanism). For diluted samples of **1–3**, behaviour similar to that of **1–3** (powder sample) were observed, thus confirming that the magnetic properties were not due to the intermolecular $Tb^{III}\cdots Tb^{III}$ interactions, as shown in Fig. S9.†[6,7] Therefore, the different magnetic behaviours observed for **1–3** is thought to be due to the symmetry of the octa-coordination environment.[4–6,9,13] Below, the relationship between the symmetry of coordination environments and the ν dependence of the ac susceptibilities are discussed.

Dynamic magnetic properties

To elucidate the details of the relaxation dynamics, ac magnetic susceptibility measurements were performed on powder samples of **1** (SP–SP) and **2** (SAP–SAP*) in a 3 Oe oscillating ac field. The in-phase (χ_M') and out-of-phase (χ_M'') signals changed in different T ranges depending on the ν in the range of 1–996 Hz, indicating that **1** and **2** are SMMs (Fig. 3 and 4, S10–S28†). The values of the energy barrier for the reversal of the magnetization (Δ) and pre-exponential factor (τ_0: the average relaxation time in response to thermal fluctuation) can be estimated from Arrhenius equation: $\tau = \tau_0 \exp(\Delta/k_BT)$,[1,2] where τ is the magnetic relaxation time, k_B is Boltzmann constant. This linear relation between $\ln(\tau)$ and T^{-1} indicates that the Orbach process (spin–phonon interaction which approximately corresponds to the Δ for thermal relaxation for the reversal of the magnetic moment) is dominant in high-T ranges. This method is highly credible for the high-T region.

χ_M'' *versus* T plots for both **1** and **2** in the ν range of 1–996 Hz barely showed any tailing, and the expected maximum value due to blocking could not be observed down to 1.8 K in an applied H_{dc} of zero (Fig. 3a, S10 and S11†). The χ_M'' did not disappear in the T region below 2 K, indicating that the magnetic moment was not frozen and that a different relaxation process, which is likely a ground state QTM process, became dominant in the low-T region. Since we have no basis for comparing Δ and τ_0 in a zero H_{dc}, we determined Δ for **1** and **2**

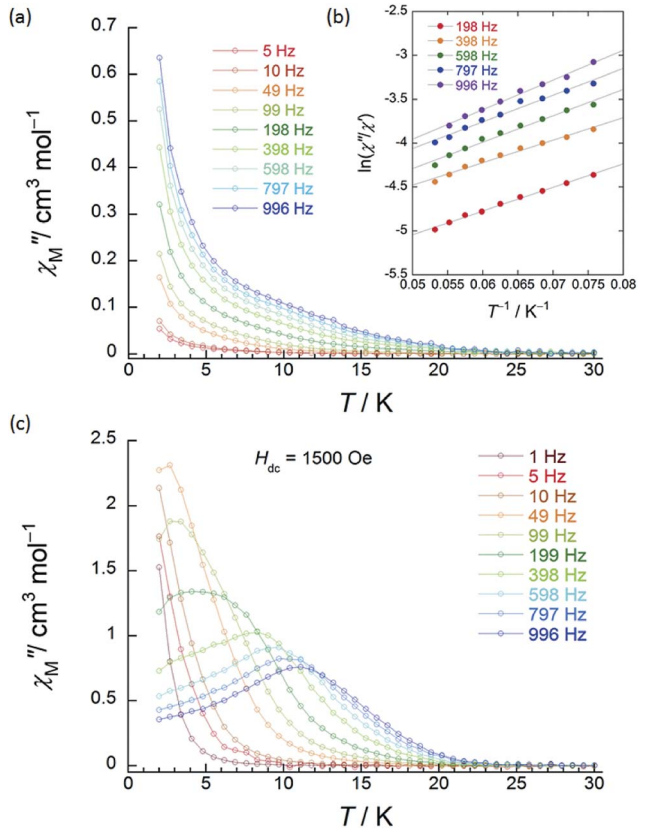

Fig. 3 Frequency (ν) and temperature (T) dependence of the ac magnetic susceptibilities (χ_M'': out-of-phase) of **1** (SP–SP). The measurements were performed in a 3 Oe ac magnetic field at the indicated frequencies in an H_{dc} of (a) zero. The solid lines are guides for eyes. (b) χ_M''/χ_M' *versus* T^{-1} (13–18 K) plot at the given ν (198–996 Hz) of the ac susceptibility data by using the Kramers–Kronig equation (eqn (S1)–(S3)†). The solid lines were fitted as described in Table S2.† (c) ν dependence of χ_M'' *versus* T in an H_{dc} of 1500 Oe. The solid lines are guides for eyes.

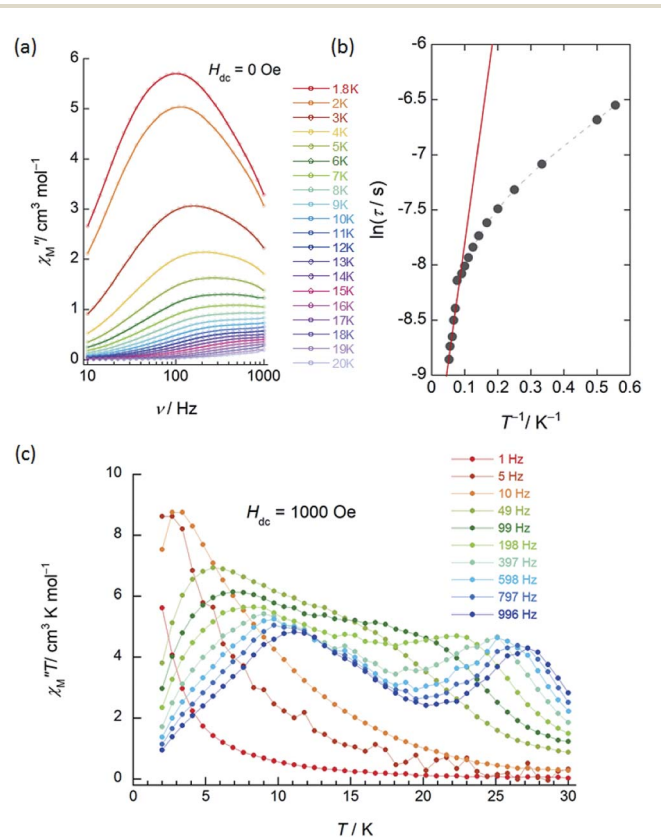

Fig. 4 Frequency (ν) and temperature (T) dependence of the ac magnetic susceptibility (χ_M'': out-of-phase) of **2** (SAP–SAP*). The measurements were performed in a 3 Oe ac magnetic field at the indicated ν. (a) ν dependence of χ_M'' measured between 1.8 and 20 K in an H_{dc} of zero. The solid lines are guides for eyes. (b) Arrhenius plots for **2** in an H_{dc} of zero. Solid lines were fitted by using the Arrhenius equation (see main text). (c) ν dependence of $\chi_M''T$ *versus* T at H_{dc} of 1000 Oe. The solid lines are guides for eyes.

from χ_M''/χ_M' *versus* T^{-1} (13–18 K) plots of the ac susceptibility data at various ν (198–996 Hz) by using the Kramers–Kronig equation (eqn (S1)–(S3)† and Fig. 4b).[14] By fitting the data, the Δ was determined to be 18–24 cm^{-1} with $\tau_0 = 10^{-6}$ to 10^{-7} s for **1** and 36–38 cm^{-1} with $\tau_0 \approx 10^{-6}$ s for **2** in a zero H_{dc}. The estimated parameters for **1** and **2** are summarized in Tables S2 and S3,† respectively.

In the case of **1** (SP–SP), in detailed H_{dc} dependent ac magnetic susceptibility (χ_M' and χ_M'') measurements at ν of 996 Hz in the T range of 2–30 K, χ_M'' showed a single maximum at 11 K in an H_{dc} of 1500 Oe (Fig. 3c and S12†). The shapes of the peaks of **1** drastically changed, and the peaks shifted to the low-T side when an H_{dc} large enough to suppress QTM was applied. The χ_M' and χ_M'' peaks were clearly shifted in different T ranges dependent on the ν (1–996 Hz) in H_{dc} of 1500 and 3000 Oe, indicating that **1** is a field-induced SMM (Fig. S13†).

In contrast to **1**, **2** (SAP–SAP*) showed clear H_{dc} field dependent character and two χ_M'' peaks appeared at 11 K and 27 K at 996 Hz and did not show H_{dc} dependence in the range of 250–5000 Oe, indicating that **2** is a field-induced SMM (Fig. S14 and S15†). However, a χ_M'' peak top for **2** was not clearly observed in the measured T range (Fig. S15b†). In order to clarify the T dependence, we prepared $\chi_M'T$ and $\chi_M''T$ graphs (Fig. 4c and S16†). The shape of the two peaks of **2** were drastically different from those of **1** and clearly shifted in different T ranges depending on ν in an H_{dc} of 1000 Oe.

This behaviour is similar to those of other dinuclear Tb^{III} complexes with slightly different structures relative to **2**, such as {(Pc)Tb(Pc)Tb[T(*p*-OMe)PP]} and [(Pc)Tb(Pc)Tb(obPc)], with different coordination environments around the asymmetric Tb^{III} sites reported by Ishikawa and co-workers.[5,9a] Our results clearly show that the two Tb^{III} ion sites (SAP and SAP* sites) are inequivalent and are in agreement with the structure of **2** (SAP–SAP*) determined using XRD and the ac susceptibility measurements. From a $\chi_M''T$ *versus* T plot, the intensity of the χ_M'' peak top at 27 K (the SAP* site of **2**) was lower in an H_{dc} of 3000 Oe. On the other hand, the intensity of the χ_M'' peak top at 11 K (the SAP site of **2**) showed ν dependence, and this behaviour is similar to that observed in a $\chi_M''T$ *versus* T plot for **2** in a zero H_{dc} (Fig. S17 and S18†). It was attributed to an Orbach process, which was observed when an H_{dc} large enough to suppress QTM ($\tau \approx 10^{-4}$ s) was applied. The Orbach process for the SAP* environment is inhibited by fast QTM and/or direct magnetic relaxation process ($\tau \approx 10^{-3}$ s).[13g,15] See the details in "the Magnetic relaxation mechanism" section.

In the case of **3** (SAP–SAP), in a χ_M'' *versus* T plot at ν of 996 Hz, only a single peak around 24 K was observed in an H_{dc} of zero.[6] These results indicate that the two $\chi_M''T$ peak top T values (11 and 27 K) at 996 Hz for **2** with an SAP–SAP* site correspond to a state that is a combination of **1** with an SP–SP site (11 K) and **3** with an SAP–SAP site (24 K), respectively (Fig. 5). Thus, it is important to study the properties of dinuclear Tb^{III} triple-decker type SMMs on the bases of crystal structure features, such as molecular contractions, *i.e.*, LF and CF of the central metal ions.

To elucidate the details of the relaxation dynamics of **1** and **2**, the ν dependence of the χ_M' and χ_M'' signals in the range of 10–996 Hz were studied at each T. Argand plots (χ_M'' *versus* χ_M') for

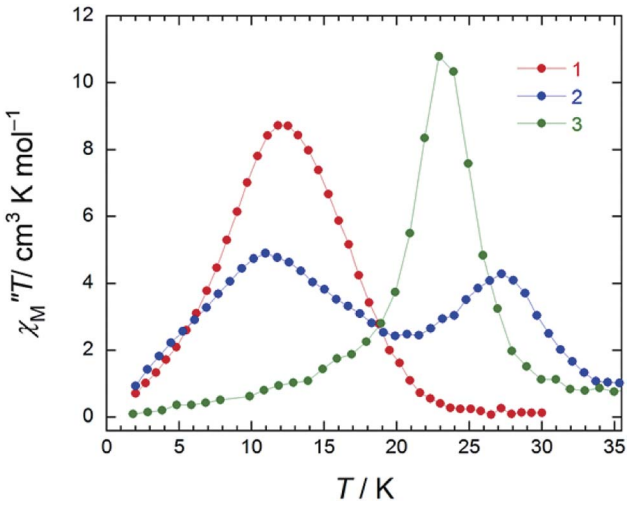

Fig. 5 Temperature (T) dependence of the ac magnetic susceptibilities (χ_M'': out-of-phase) of **1–3** ($\chi_M''T$ *versus* T plot). The measurements were performed in a 3 Oe ac magnetic field at the indicated frequencies (996 Hz) in an H_{dc} of 1000 Oe for **1** (SP–SP), 1500 Oe for **2** (SAP–SAP*), and zero for **3** (SAP–SAP), respectively. In order to suppress QTM, we applied an H_{dc} for **1** and **2** (see main text). The solid lines are guides for eyes.

1 were partially semicircular in shape in an H_{dc} of zero in the T range of 4–16 K (Fig. S19†). In the case of the χ_M'' signals for **1** in the range of 10–996 Hz, the expected maximum value due to blocking could not be observed down to 1.8 K in an applied H_{dc} of zero (Fig. S19b†). On the contrary, below 10 K, a small shoulder peak in the range of 10–100 Hz was observed. A χ_M'' peak top T of 5 K was observed when $H_{dc} > 200$ Oe (Fig. S20b†). The shape of the χ_M'' peaks for **1** drastically changed and shifted to the low-ν side when an H_{dc} large enough to suppress QTM was applied, which will be described in detail below (Fig. 8).

The obtained τ values of **1** are plotted as a function of T^{-1} in Fig. S21.† We observed QTM (T-independent regime for τ) with a fast τ below 10 K. These results confirm that QTM *via* the presence of off-diagonal LF terms in SP–SP environments is not suppressed in sharp contrast to that of **3** (SAP–SAP).[6] Ishikawa and co-workers have reported that the ground state of an SP site has a high probability of QTM in comparison to an SAP one due to the presence of off-diagonal LF terms.[4,9a,13] In the above case, the τ values at 5 K for **1–3** in an H_{dc} of zero follow the order: **1** with SP–SP site (4.1×10^{-5} s) < **2** with SAP–SAP* sites (5.6×10^{-4} s) < **3** with SAP–SAP sites (1.8×10^{-2} s) (Table S4†). This coordination relationship is also reflected in the τ of the QTM process at low-T region.

In order to study the field-induced SMM properties, the ν dependence of the χ_M' and χ_M'' signals for **1** in the range of 10–996 Hz were measured at each T (4–16 K) in H_{dc} of 1500 and 3000 Oe (Fig. S22 and S23†). From Argand plots in H_{dc} of 1500 and 3000 Oe, which were made using a generalized Debye model (eqn (S4)–(S6)†), the magnetic relaxations of **1** with SP–SP geometry showed a single component process.[16] The obtained τ values are plotted as a function of T^{-1} in Fig. S24.† The T-independent regime for QTM was restrained, and there were clear signs of the T-dependent regime for the Orbach process.

The Δ was estimated from a χ_M'' *versus* ν plot to be 32 cm^{-1}, and a τ_0 value of 3.97×10^{-6} s was obtained from an Arrhenius plot using $\tau = \tau_0 \exp(\Delta/k_BT)$ for **1** in an H_{dc} of 1500 and 3000 Oe in the T range of 11–16 K (Fig. S24†). These results confirm that the QTM is suppressed in an H_{dc} and that the direct process is enhanced. This is clear evidence that τ of **1** depends heavily on T and H_{dc}.

On the other hand, as shown in Fig. S25,† Argand plots for **2** were semicircular in an H_{dc} of zero in the T range of 1.8–20 K and could be analyzed using a generalized Debye model (eqn (S4)–(S6)†).[16] The obtained τ values of **2** are plotted as a function of T^{-1} in Fig. 4b. We did not observe pure QTM (T-independent regime for τ), and the T-dependent regime for τ occurred under 10 K. These results confirm that pure QTM *via* the SAP–SAP* environments of **2** is suppressed as it is in **3** with SAP–SAP sites.[6] The solid line represents a least-squares fit by using an Arrhenius equation with the following kinetic parameters: $\Delta = 15$ cm^{-1} and $\tau_0 = 4.8 \times 10^{-5}$ s (Fig. 4b). These values have similar orders of magnitude as those obtained by using the Kramers–Kronig equation (Table S3†).

On the other hand, the T-dependent regime for τ in the low-T region appears to involve thermally assisted QTM *via* a doublet ground state, a direct process and/or a Raman process, which are difficult to separate from each other.[13d,15] Together with the Arrhenius plot of the data from $\chi_M''T$ *versus* T (Fig. S16b†) and χ_M'' *versus* ν plots for **2** in an H_{dc} of 1000 Oe (Fig. 4c and S26†), Δ was estimated to be 60 cm^{-1} with τ_0 of 3.48×10^{-6} s (SAP site: blue circle in Fig. 6) and 162 cm^{-1} with 3.16×10^{-8} s (SAP* site: red open circle in Fig. 6) in the T range of 18–29 K. Furthermore, Argand plots for **2** were partially semicircular in shape for the magnetic relaxation process in an H_{dc} of 3000 Oe in the T range of 4–17 K (Fig. S27†). Similar irregularity was observed in the Argand plots when $T < 6$ K but in an applied $H_{dc} > 500$ Oe (Fig. S28†).

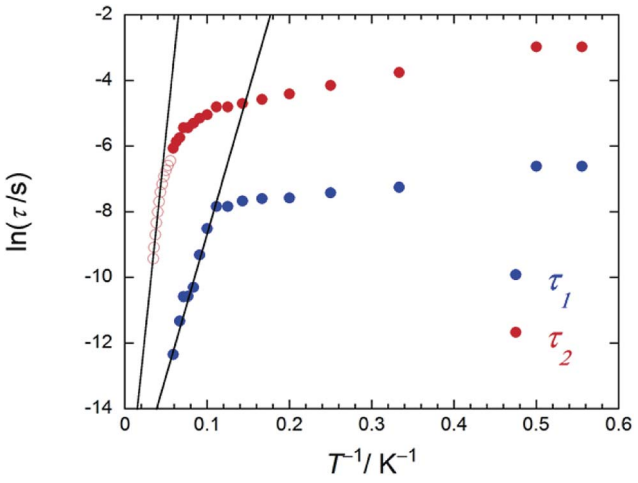

Fig. 6 An Arrhenius plot of **2** (SAP–SAP*), where the magnetic relaxation time τ (blue and red circles) were obtained from χ_M'' *versus* ν plots (Fig. S26b†) at T between 1.8 and 20 K in an H_{dc} of 1000 Oe and the red open circles were obtained from peak top T of $\chi_M''T$ *versus* T plots (Fig. 4c) at T between 22 and 27 K in an H_{dc} of 1000 Oe. τ was obtained from the least-squares fitting using a generalized Debye model (eqn (S4)–(S6)†) and an extended Debye model (eqn (S8)–(S10)†).

In order to elucidate the relationship between the geometry and LF, we examined the correlation between the twist angle (φ) and Δ (Fig. 7). Δ *versus* φ plots for **1–3** and $[TbPc_2]^-$ complex showed linear relationships. Above 10 K, the lowest excitation in the energy gap between the ground and first excited state levels of each SMM are approximately the same magnitude as the obtained Δ values because the intramolecular Tb^{III}–Tb^{III} interactions have little effect on the LF (Fig. S29†). As previously stated, the molecular geometry is related to the mixing of off-diagonal LF terms.[4,5,9,13] In other words, the degree of mixing of the off-diagonal LF terms increases from the D_{4d} ($[TbPc_2]^-$ complex with $\varphi \approx 45°$) to D_{4h} (**1** with $\varphi \approx 4°$). Thus, Δ for the D_{4h} geometry becomes narrower than that for the D_{4d} one due to the influence of LF parameters. This agrees with earlier studies.[2,4,5,9,13i,j] In addition, there is a slight deviation from linearity in the plot of Δ due to distortions in the molecular geometry, such as longitudinal contraction of the coordination environment.[4e,i] Selected geometry and SMM information for **1–3** and related SMM are listed in Table S5.†

Magnetic relaxation mechanism

The magnetic relaxation processes in dc magnetic fields can be explained by applying the Landau–Zener–Stükelberg (LZS) model of the ground state $\pm J_z$ levels.[1,2,17] Probability P of the adiabatic change can be obtained from the relationship between Δ_{tunnel} and the magnetic field sweep rate. The fast spin reversal between the $\pm J_z$ levels due to the adiabatic process is QTM. Relaxation *via* a direct process causes the release of a phonon (h_ω) when the spin flips in a nonadiabatic process. The probability of nonadiabatic process ($1 - P$) shows that the spin is not maintained with changes in the magnetic field sweep rate. This is thought to be the basis for the magnetic relaxation mechanism of **1–3** in the low-T region.

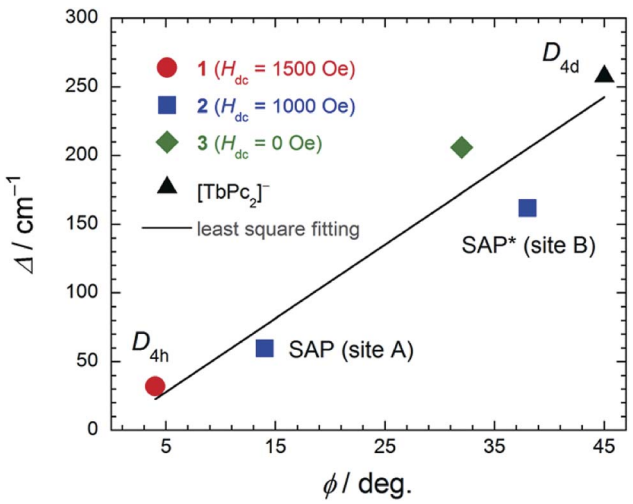

Fig. 7 The relationship between the twist angle (φ) and the energy barrier for the reversal of the magnetization (Δ). The experimental data for $[TbPc_2]^-$ complex with D_{4d} geometry from ref. 4*c* and **3** from ref. 7*e*. In order to suppress QTM, we applied an H_{dc} for **1** and **2** (see main text). The solid line is a guide for eyes.

In a previous study on SMM **3** (SAP–SAP), we determined the ground state from the magnetic heat capacity (C_m) in an H_{dc} (Fig. S30†).[6] When two Tb^{III} ions are in close proximity to each other, ferromagnetic ($|\pm6, \pm6\rangle$) and antiferromagnetic states ($|\pm 6, \mp6\rangle$) form, and these states are energetically separated by the f–f interactions between the Tb^{III} ions. Broadening of the C_m peak with an increase in H_{dc} shows that the $J_z = |-6, -6\rangle$, $|+6, +6\rangle$ and $J_z = |-6, +6\rangle$, $|+6, -6\rangle$ energy levels of the dinuclear Tb^{III} system are split by Zeeman energy. The magnetic axes of the ground state at the Tb^{III} sites are parallel to each other and have ferromagnetic dipole–dipole interactions among the magnetic moments ($J_z = |\pm6, \pm6\rangle$). The dependence of the C_m of **3** on H_{dc} aligned along the magnetic easy axis could be reproduced theoretically (Fig. S30d†). The degenerate $J_z = |\pm6, \pm6\rangle$ is split into $J_z = |-6, -6\rangle$ and $J_z = |+6, +6\rangle$ in an H_{dc} (Zeeman splitting). Thus, the crossing point at around ±4000 Oe is due to level crossing of the $J_z = |\pm6, \mp6\rangle$ state and $J_z = |+6, +6\rangle$ state. Furthermore, in the micro-SQUID experiments, **3** clearly exhibited a butterfly-shaped hysteresis loop with the field applied along the easy magnetization axis (Fig. S30b†).[6] In the up sweep, the magnetization jump around ±3500 Oe is due to level crossing of the doublet ground state between the $J_z = |\pm6, \mp6\rangle$ state and $J_z = |+6, +6\rangle$ state.

Ishikawa and co-workers have obtained the Zeeman plots, where in the presence of the nuclear spin of $I_z = \pm3/2, \pm1/2$ with $J_z = \pm6$ of the dinuclear Tb^{III} system, pure QTM in an H_{dc} of zero is forbidden because of the absence of mixing between the $|\pm6, \mp6\rangle$ and $|\pm6, \pm6\rangle$ states.[9a] Therefore, there is no crossover between the QTM and direct processes. At around ±3500 Oe, although QTM is possible, the direct process is a possible relaxation pathway in such a strong H_{dc} at low-T (Fig. 8c and S30b†). Therefore, we have reported that **3** shows pure QTM and a direct process in H_{dc} of around 3500 Oe, which is consistent with the Zeeman diagrams. Furthermore, we can explain the dual magnetic relaxation mechanism of **2** (SAP–SAP*) using Zeeman diagrams.

On the other hand, below 18 K, the Argand plots for **2** showed two sets of irregular semicircular shapes for the dual magnetic relaxation processes in an H_{dc} of 1000 Oe (Fig. S26†). In other words, the magnetic relaxation splits from a one-component system into a two-component system (τ_1: high-frequency part and τ_2: low-frequency part) in an H_{dc} similar to the case of **3**. In order to understand the different relaxation mechanisms corresponding to the two observed peaks, an extended Debye model (eqn (S8)–(S10)†) was used to fit the values of τ_1 and τ_2.[6,8a] τ_1 and τ_2 are plotted as a function of T^{-1} in Fig. 6. There are two different T regions. Above 18 K, the relaxation follows a thermally-activated mechanism, such as the Orbach process, whereas at lower temperatures (<10 K), a gradual crossover to a T-independent regime for τ_1 and T-dependent regime for τ_2 occurs. Similar behaviour was observed for **3** (SAP–SAP), and this is clear evidence that the magnetic relaxation mechanism depends heavily on the ground state properties of the Tb^{III} ions in the dinuclear systems below 10 K (Fig. 2).[6,7]

To corroborate the relationship between the dual magnetic relaxation process in the dinuclear Tb^{III} complexes **1–3** in the low-T region and the octa-coordination environments, the ν dependence of χ_M' and χ_M'' in the range of 10–996 Hz were conducted at 5 K in several H_{dc}.[6,7] In the case of the Argand plots

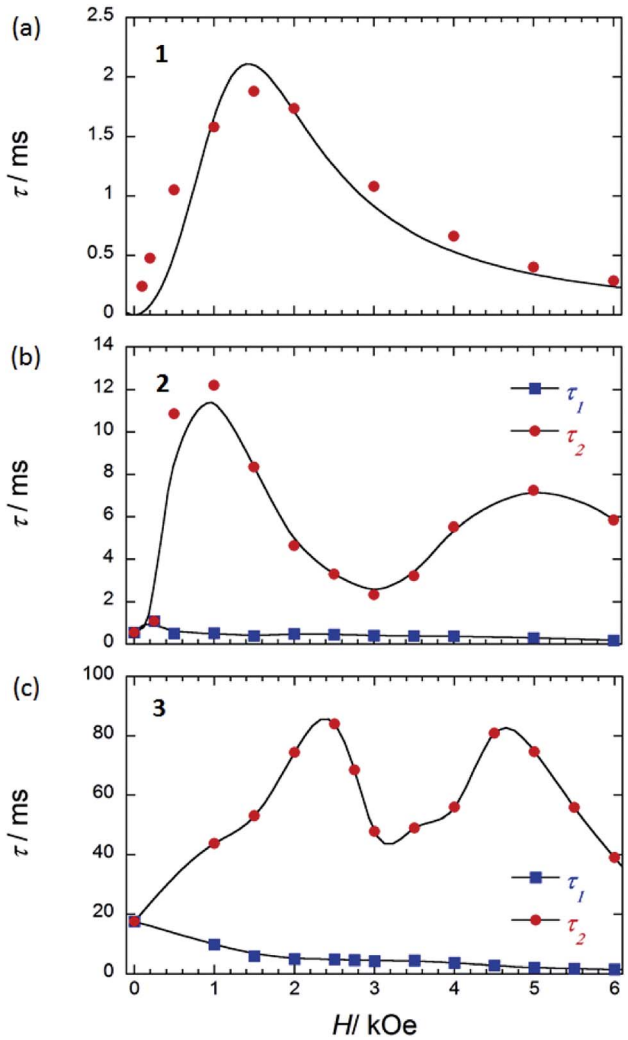

Fig. 8 τ *versus* H for (a) **1** (SP–SP), (b) **2** (SAP–SAP*), and (c) **3** (SAP–SAP)[6] at 5 K. τ was obtained from the least-squares fitting using an extended Debye model (eqn (S8)–(S10) and Fig. S20 and S28†). The order of the maximum values of τ (red circle) are different from each other. See main text. The solid lines are guides for eyes.

for **2** in an H_{dc} up to 6000 Oe at 5 K (Fig. S28†), the magnetic relaxation splits from a one-component system into a two-component system (τ_1 and τ_2). τ_1 ($\sim10^{-4}$ s) did not change in the range of 0–6000 Oe. On the other hand, τ_2 fluctuated with an "M" shaped curve (Fig. 8b) in the same ν range. τ_2 increased from 250 Oe and became a maximum of $\sim10^{-2}$ s in an H_{dc} of 1000 Oe ($H_{\tau_2,max}$). These results confirm that the QTM is suppressed in an H_{dc} of 1000 Oe, and the direct process is enhanced. When H_{dc} > 1000 Oe, the magnitude of τ_2 decreased to a minimum value ($\sim10^{-3}$ s) in H_{dc} of ~3000 Oe ($H_{\tau_2,min}$). Then τ_2 began to increase again to a second maximum in an H_{dc} of 5000 Oe, followed by another decrease. These results confirm that the QTM is induced in the H_{dc} range of 1000–5000 Oe, and the direct process and QTM are enhanced due to Zeeman splitting of $J_z = |\pm6, \pm6\rangle$ and level crossing of the doublet ground state between the $J_z = |\pm6, \mp6\rangle$ state and $J_z = |+6, +6\rangle$ state around 3000 Oe, respectively. The two levels of the lines in the energy diagrams are broadened because the coupled states

are finely split by hyperfine coupling (*I*–*J*) and the interactions between the spins (f–f), which are due to absorption and/or emission of phonons (spin–phonon interactions).[4,6] Thus, the width of level crossing of the doublet ground state between the $J_z = |\pm 6, \mp 6\rangle$ and $J_z = |+6, +6\rangle$ states expanded in the H_{dc} range of 1000–5000 Oe.[7e] Therefore, we believe that the magnetic relaxation process in an H_{dc} can be explained using Zeeman diagrams. By comparing the H_{dc} dependence of τ for the dinuclear Tb^{III} system, we found that the octa-coordination geometries with SAP–SAP* and SAP–SAP sites affected the H_{dc} regions where QTM was active.

In contrast to **2** and **3** (Fig. 8b and c), **1** with SP–SP sites exhibited only a single magnetic relaxation process (Fig. 8a), which could be described by using a generalized Debye model (eqn (S4)–(S6)†). The order of τ (10^{-4} s) increased from 250 Oe, reaching a maximum value of $\sim 10^{-3}$ s in an H_{dc} of 1500 Oe ($H_{\tau,max}$). These results confirm that the QTM is suppressed in an $H_{dc} = 1500$ Oe and that the direct process is enhanced. When $H_{dc} > 1500$ Oe, the order of magnitude of τ decreased to a minimum value of $\sim 10^{-4}$ s in an H_{dc} of 6000 Oe. These results confirm that the QTM is suppressed up to an H_{dc} of 6000 Oe and that the direct process is enhanced. The ground state properties of **1** are completely different from those of **2** and **3**. The ground state of **2** and **3** undergo a level crossing to give rise to a dual magnetic relaxation phenomenon, whereas **1** does not (Fig. 8a and S30†). This is consistent the differences in the values of Δ_{tunnel} in the ground states of the SP and SAP environments.[9a] The differences are due to the differences in the ground state brought about by the symmetry of octa-coordination geometries and can be explained on the bases of the Zeeman diagrams.

Conclusions

The relationship between the octa-coordination environment and the SMM properties of **1** (SP–SP) and **2** (SAP–SAP*) with different octa-coordination environments are discussed in comparison to **3** (SAP–SAP). The SMM behaviours of the three complexes were explained by using X-ray crystallography and static and dynamic susceptibility measurements.

The relaxation dynamics of **1** and **2** indicate that they are field-induced SMMs because the QTM is enhanced by the presence of off-diagonal LF terms (B_k^q; $q \neq 0$). Both **2** and **3** undergo dual magnetic relaxation processes in an H_{dc}, whereas **1** undergoes only a single magnetic relaxation process. The differences are due to the differences in the ground state of the respective octa-coordination geometries and can be explained on the bases of the Zeeman diagrams. Thus, the dual magnetic relaxation properties of dinuclear Tb^{III} complexes can be tuned by changing the strength of the mixing of fourth-range extra-diagonal parameters using the octa-coordination environments, and thus, we must carefully design the dinuclear Tb^{III} triple-decker complexes to control the dual magnetic relaxation mechanisms.

In addition, we demonstrated that there was a linear relationship between the twist angle (φ) and the energy barrier for the reversal of the magnetization (Δ). Qualitatively, this result is consistent with the degree of the mixing of off-diagonal LF terms due to the symmetry of the octa-coordination environment. Detailed theoretical calculations will make it possible to fully elucidate the relationship between LF and SMM properties in detail.

Finally, the dual magnetic relaxation mechanisms are related the two energy gap in the doublet ground state in the dinuclear Tb^{III} ions with ferromagnetic dipolar interactions and the octa-coordination geometry because the SAP–SAP sites have axial components in the LF terms and because the SP–SP sites have not only the axial LF terms but also the off-diagonal LF terms.

Acknowledgements

This work was financially supported by a Grant-in-Aid for Scientific Research (S) (Grant No. 20225003, MY) and Grant-in-Aid for Young Scientists (B) (grant No. 24750119, KK) and Scientific Research (C) (grant No. 15K05467, KK) from the Ministry of Education, Culture, Sports, Science, and Technology (MEXT) and CREST, JST, Japan.

Notes and references

1 (*a*) R. Sessoli, D. Gatteschi, A. Caneschi and M. A. Novak, *Nature*, 1993, **365**, 141; (*b*) R. Sessoli and D. Gatteschi, *Angew. Chem., Int. Ed.*, 2003, **42**, 268; (*c*) D. Gatteschi, R. Sessoli and J. Villain, *Molecular Nanomagnets*, Oxford University Press, Oxford, U.K., 2006.

2 (*a*) X.-Y. Wang, C. Avendaño and K. R. Dunbar, *Chem. Soc. Rev.*, 2011, **40**, 3212; (*b*) J. D. Rinehart and J. R. Long, *Chem. Sci.*, 2011, **2**, 2078; (*c*) *Molecular Cluster Magnets (World Scientific Series in Nanoscience and Nanotechnology-Vol. 3)*, ed. R. E. P. Winpenny, World Scientific Publishing Co. Pte. Ltd., USA, 2011; (*d*) D. N. Woodruff, R. E. P. Winpenny and R. A. Layfield, *Chem. Rev.*, 2013, **113**, 5110; (*e*) F. Habib and M. Murugesu, *Chem. Soc. Rev.*, 2013, **42**, 3278; (*f*) K. S. Pedersen, J. Bendix and R. Clérac, *Chem. Commun.*, 2014, **50**, 4396; (*g*) *Introduction to Molecular Magnetism: From Transition Metals to Lanthanides*, ed. C. Benelli and D. Gatteschi, Wiley-VCH, Germany, 2015; (*h*) *Lanthanides and Actinides in Molecular Magnetism*, ed. R. A. Layfield and M. Murugesu, Wiley-VCH, Germany, 2015; (*i*) A. A., Molecular Nanomagnets and Related Phenomena, *Struct. Bonding*, 2015, **164**; (*j*) S. T. Liddle and J. van Slageren, *Chem. Soc. Rev.*, 2015, **44**, 6655.

3 (*a*) A. Candini, S. Klyatskaya, M. Ruben, W. Wernsdorfer and M. Affronte, *Nano Lett.*, 2011, **11**, 2634; (*b*) M. Urdampilleta, S. Klyatskaya, J.-P. Cleuziou, M. Ruben and W. Wernsdorfer, *Nat. Mater.*, 2011, **10**, 502; (*c*) S. Bertaina, S. Gambarelli, T. Mitra, B. Tsukerblat, A. Muller and B. Barbara, *Nature*, 2008, **453**, 203; (*d*) L. Bogani and W. Wernsdorfer, *Nat. Mater.*, 2008, **7**, 179; (*e*) E. Burzurí, F. Luis, B. Barbara, R. Ballou, E. Ressouche, O. Montero, J. Campo and S. Maegawa, *Phys. Rev. Lett.*, 2011, **107**, 097203; (*f*) W. Wernsdorfer and R. Sessoli, *Science*, 1999, **284**, 133; (*g*) M. N. Leuenberger and D. Loss, *Nature*, 2001, **410**, 789.

4 (*a*) N. Ishikawa, M. Sugita, T. Ishikawa, S. Koshihara and Y. Kaizu, *J. Am. Chem. Soc.*, 2003, **125**, 8694; (*b*) N. Ishikawa, M. Sugita and W. Wernsdorfer, *Angew. Chem., Int. Ed.*, 2005, **44**, 2931; (*c*) N. Ishikawa, M. Sugita, T. Ishikawa, S. Koshihara and Y. Kaizu, *J. Phys. Chem. B*, 2004, **108**, 11265; (*d*) N. Ishikawa, *Polyhedron*, 2007, **26**, 2147; (*e*) S. Takamatsu and N. Ishikawa, *Polyhedron*, 2007, **26**, 1859; (*f*) N. Ishikawa, M. Sugita, T. Okubo, N. Tanaka, T. Iino and Y. Kaizu, *Inorg. Chem.*, 2003, **42**, 2440; (*g*) N. Ishikawa, *J. Phys. Chem. A*, 2003, **107**, 5831; (*h*) N. Ishikawa and Y. Kaizu, *Coord. Chem. Rev.*, 2002, **226**, 93; (*i*) S. Takamatsu, T. Ishikawa, S. Koshihara and N. Ishikawa, *Inorg. Chem.*, 2007, **46**, 7250.

5 (*a*) N. Ishikawa, S. Otsuka and Y. Kaizu, *Angew. Chem., Int. Ed.*, 2005, **44**, 731; (*b*) N. Ishikawa, T. Iion and Y. Kaizu, *J. Am. Chem. Soc.*, 2002, **124**, 11440; (*c*) N. Ishikawa, T. Iino and Y. Kaizu, *J. Phys. Chem. A*, 2002, **106**, 9543; (*d*) Y. Lan, S. Klyatskaya, M. Ruben, O. Fuhr, W. Wernsdorfer, A. Candini, V. Corradini, A. L. Rizzini, U. del Pennino, F. Troiani, L. Joly, D. Klar, H. Wende and M. Affrontef, *J. Mater. Chem. C*, 2015, **3**, 9794.

6 K. Katoh, T. Kajiwara, M. Nakano, Y. Nakazawa, W. Wernsdorfer, N. Ishikawa, B. K. Breedlove and M. Yamashita, *Chem.–Eur. J.*, 2011, **17**, 117.

7 (*a*) K. Katoh, H. Isshiki, T. Komeda and M. Yamashita, *Coord. Chem. Rev.*, 2011, **255**, 2124; (*b*) K. Katoh, Y. Horii, N. Yasuda, W. Wernsdorfer, K. Toriumi, B. K. Breedlove and M. Yamashita, *Dalton Trans.*, 2012, **41**, 13582; (*c*) T. Morita, K. Katoh, B. K. Breedlove and M. Yamashita, *Inorg. Chem.*, 2013, **52**, 13555; (*d*) M. Damjanovic, K. Katoh, M. Yamashita and M. Enders, *J. Am. Chem. Soc.*, 2013, **135**, 14349; (*e*) Y. Horii, K. Katoh, N. Yasuda, B. K. Breedlove and M. Yamashita, *Inorg. Chem.*, 2015, **54**, 3297.

8 (*a*) N. Domingo, F. Luis, M. Nakano, M. Muntó, J. Gómez, J. Chaboy and N. Ventosa, *Phys. Rev. B: Condens. Matter Mater. Phys.*, 2009, **79**, 214404–214411; (*b*) D. Weismann, Y. Sun, Y. Lan, G. Wolmershäuser, A. K. Powell and H. Sitzmann, *Chem.–Eur. J.*, 2011, **17**, 4700; (*c*) Y.-N. Guo, G.-F. Xu, P. Gamez, L. Zhao, S.-Y. Lin, R. Deng, J. Tang and H.-J. Zhang, *J. Am. Chem. Soc.*, 2010, **132**, 8538; (*d*) S.-D. Jiang, B.-W. Wang, H.-L. Sun, Z.-M. Wang and S. Gao, *J. Am. Chem. Soc.*, 2011, **133**, 4730; (*e*) M. Gonidec, F. Luis, À. Vílchez, J. Esquena, D. B. Amabilino and J. Veciana, *Angew. Chem., Int. Ed.*, 2010, **49**, 1623; (*f*) H. Wang, T. Liu, K. Wang, C. Duan and J. Jiang, *Chem.–Eur. J.*, 2012, **18**, 7691; (*g*) D. Pinkowicz, M. Ren, L.-M. Zheng, S. Sato, M. Hasegawa, M. Morimoto, M. Irie, B. K. Breedlove, G. Cosquer, K. Katoh and M. Yamashita, *Chem.–Eur. J.*, 2014, **20**, 12502; (*h*) F. Pointillart, T. Guizouarn, B. Lefeuvre, S. Golhen, O. Cador and L. Ouahab, *Chem.–Eur. J.*, 2015, **21**, 16929.

9 (*a*) S. Sakaue, A. Fuyuhiro, T. Fukuda and N. Ishikawa, *Chem. Commun.*, 2012, **48**, 5337; (*b*) D. Tanaka, T. Inose, H. Tanaka, S. Lee, N. Ishikawa and T. Ogawa, *Chem. Commun.*, 2012, **48**, 7796; (*c*) H. Wang, K. Wang, J. Tao and J. Jiang, *Chem. Commun.*, 2012, **48**, 2973; (*d*) J. Kan, H. Wang, W. Sun, W. Cao, J. Tao and J. Jiang, *Inorg. Chem.*, 2013, **52**(15), 8505; (*e*) K. Wang, S. Zeng, H. Wang, J. Dou and J. Jiang, *Inorg. Chem. Front.*, 2014, **1**, 167.

10 (*a*) D. Chabach, M. Lachkar, A. De Cian, J. Fischer and R. Weiss, *New J. Chem.*, 1992, **16**, 431; (*b*) T.-H. Tran-Thi, T. A. Mattiolit, D. Chabach, A. De Cian and R. Weiss, *J. Phys. Chem.*, 1994, **98**, 8279.

11 (*a*) K. Takahashi, M. Itoh, Y. Tomita, K. Nojima, K. Kasuga and K. Isa, *Chem. Lett.*, 1993, 1915; (*b*) K. Kasuga, M. Ando, H. Morimoto and M. Isa, *Chem. Lett.*, 1986, 1095; (*c*) A. De Cian, M. Moussavi, J. Fischer and R. Weiss, *Inorg. Chem.*, 1985, **24**, 3162; (*d*) J. L. Paillaud, M. Drillon, A. De Cian, J. Fischer, R. Weiss and G. Villeneuve, *Phys. Rev. Lett.*, 1991, **67**, 244.

12 (*a*) G. M. Sheldrick, *SHELX-97, Program for Crystal Structure Analysis*, Universität Göttingen, Germany, 1997; (*b*) C. F. Macrae, P. R. Edgington, P. McCabe, E. Pidcock, G. P. Shields, R. Taylor, M. Towler and J. van de Streek, *J. Appl. Crystallogr.*, 2006, **39**, 453.

13 (*a*) D. Schmitt, *J. Phys.*, 1986, **47**, 677; (*b*) J. Sievers, *Z. Phys. B: Condens. Matter Quanta*, 1982, **45**, 289; (*c*) K. W. H. Stevens, *Proc. Phys. Soc., London, Sect. A*, 1952, **65**, 209; (*d*) A. Abragam and B. Bleaney, *Electron Paramagnetic Resonance of Transition Ions*, Oxford University Press, London, 1970; (*e*) L. Sorace, C. Benelli and D. Gatteschi, *Chem. Soc. Rev.*, 2011, **40**, 3092; (*f*) C. Görller-Walrand and K. Binnemans, *Handbook on the physics and chemistry of rare earths*, ed. K. A. Gschneidner Jr and E. LeRoy, Elsevier, Amsterdam, 1996, 23, p. 121; (*g*) J.-L. Liu, Y.-C. Chen, Y.-Z. Zheng, W.-Q. Lin, L. Ungur, W. Wernsdorfer, L. F. Chibotaru and M.-L. Tong, *Chem. Sci.*, 2013, **4**, 3310; (*h*) X.-C. Huang, V. Vieru, L. F. Chibotaru, W. Wernsdorfer, S.-D. Jiang and X.-Y. Wang, *Chem. Commun.*, 2015, **51**, 10373; (*i*) J. J. Baldovi, J. J. Borrás-Almenar, J. M. Clemente-Juan, E. Coronado and A. Gaita-Ariño, *Dalton Trans.*, 2012, **41**, 13705; (*j*) L. F. Chibotaru, *Struct. Bonding*, 2015, **164**, 185.

14 (*a*) F. Luis, J. Bartolomé, J. F. Fernández, J. Tejada, J. M. Hernández, X. X. Zhang and R. Ziolo, *Phys. Rev. B: Condens. Matter*, 1997, **55**, 11448; (*b*) J. Bartolomé, G. Filoti, V. Kuncser, G. Schinteie, V. Mereacre, C. E. Anson, A. K. Powell, D. Prodius and C. Turta, *Phys. Rev. B: Condens. Matter Mater. Phys.*, 2009, **80**, 014430; (*c*) J. Ferrando-Soria, D. Cangussu, M. Eslava, Y. Journaux, R. Lescouëzec, M. Julve, F. Lloret, J. Pasán, C. Ruiz-Pérez, E. Lhotel, C. Paulsen and E. Pardo, *Chem.–Eur. J.*, 2011, **17**, 12482; (*d*) I. A. Gass, B. Moubaraki, S. K. Langley, S. R. Batten and K. S. Murray, *Chem. Commun.*, 2012, **48**, 2089.

15 (*a*) I. Waller, *Z. Phys.*, 1932, **79**, 370; (*b*) J. H. Van Vleck, *J. Chem. Phys.*, 1939, **7**, 72; (*c*) J. H. Van Vleck, *Phys. Rev.*, 1940, **57**, 426; (*d*) R. de and L. Kronig, *Physica*, 1939, **6**, 33; (*e*) R. Orbach, *Proc. Phys. Soc.*, 1961, **77**, 821; (*f*) C. B. P. Finn, R. Orbach and W. P. Wolf, *Proc. Phys. Soc.*, 1961, **77**, 261; (*g*) R. L. Carlin, *Magnetochemistry*, Springer, Berlin, 1986.

16 K. S. Cole and R. H. Cole, *J. Chem. Phys.*, 1941, **9**, 341.

17 (*a*) L. D. Landau, *Phys. Z. Sowjetunion*, 1932, **2**, 46; (*b*) C. Zener, *Proc. R. Soc. London, Ser. A*, 1932, **137**, 696; (*c*) E. C. G. Stückelberg, *Helv. Phys. Acta*, 1932, **5**, 369.

